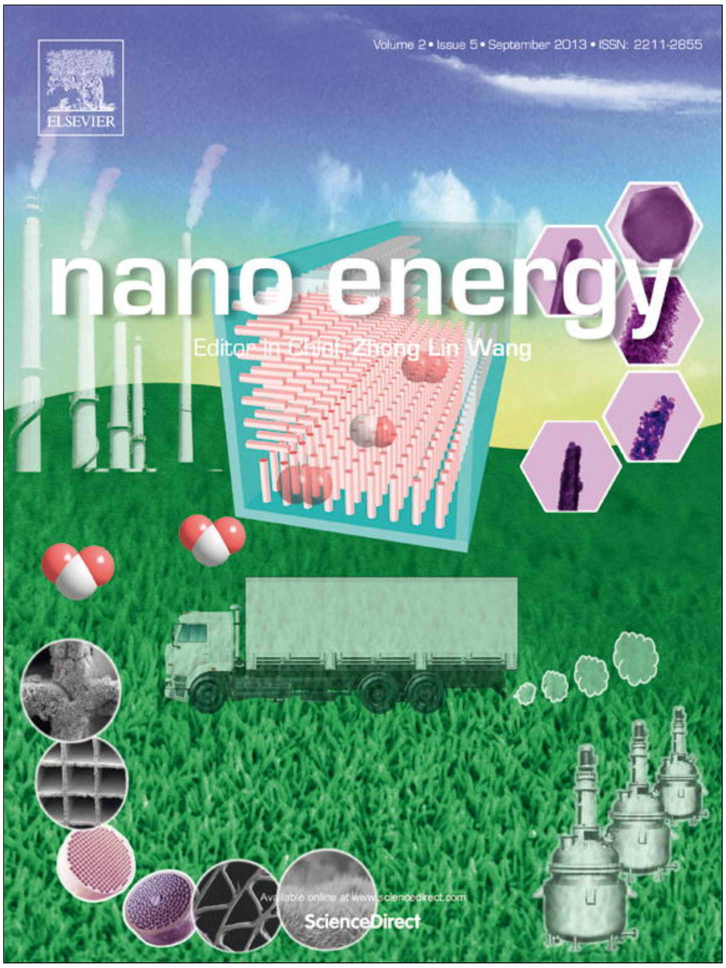
ELSEVIER
Volume 2 • Issue 5 • September 2013 • ISSN: 2211-2855
nano energy
Editor-in-Chief: Zhong Lin Wang
Available online at www.sciencedirect.com
ScienceDirect

Nano Energy (2013) 2, 769–778

Available online at www.sciencedirect.com

ScienceDirect

journal homepage: www.elsevier.com/locate/nanoenergy

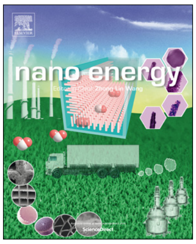

RAPID COMMUNICATION

Homogenous incorporation of SnO_2 nanoparticles in carbon cryogels via the thermal decomposition of stannous sulfate and their enhanced lithium-ion intercalation properties

Ming Zhang[a,b], Yanwei Li[b], Evan Uchaker[b], Stephanie Candelaria[b], Laifa Shen[b], Taihong Wang[a,*], Guozhong Cao[b,**]

[a] *Key Laboratory for Micro-Nano Optoelectronic Devices of Ministry of Education, and State Key Laboratory for Chemo/Biosensing and Chemometrics, Hunan University, Changsha 410082, China*
[b] *Department of Materials Science and Engineering, University of Washington, Seattle, WA 98195, United States*

Received 30 December 2012; received in revised form 28 January 2013; accepted 28 January 2013
Available online 11 February 2013

KEYWORDS
Tin oxides;
Carbon cryogels;
Lithium ion batteries;
Thermal decomposition

Abstract
An impregnation-calcination method based on the thermal decomposition of stannous sulfate is developed to prepare carbon cryogel-tin oxide nanocomposites with less impurity for anode materials of lithium-ion batteries. Structural characterization reveals that the tin oxide nanoparticles, arising from the decomposition of stannous sulfate, are homogeneously distributed inside the pores of carbon cryogels. The detail results demonstrate that carbon cryogels with large specific surface area, large porosity, and small mesopores are beneficial to the deposition of tin oxide nanoparticles. As a result, carbon cryogel-tin oxide nanocomposites with optimized structures show a discharge capacity of 590 mA h/g after 50 cycles, much higher than that of either carbon cryogels, pure tin oxides or their mechanical mixture. The superior electrochemical properties of carbon cryogel-tin oxide nanocomposites could be attributed to their novel microstructures and the synergistic effects between carbon cryogels and tin oxide.

Introduction

Owing to their excellent properties and abundant resources, carbon materials are used in a variety of fields, such as

---

[*] Corresponding author.
[**] Corresponding author. Tel.: +1 206 616 9084; fax: +1 206 543 3100.
E-mail addresses: thwang@iphy.ac.cn (T. Wang), gzcao@u.washington.edu, gzcao@uw.edu (G. Cao).

2211-2855/$ - see front matter © 2013 Elsevier Ltd. All rights reserved.
http://dx.doi.org/10.1016/j.nanoen.2013.01.009

supercapacitors [1-6], fuel cells [7], lithium-ion batteries (LIBs) [8-14], catalyst carriers [15], and conductive materials [16]. Especially in energy fields, carbon materials have been widely used and drawn much attention for further development in recent years [17,18]. For example, carbon nanotubes and graphene have been investigated by many researchers for various energy-related applications [8,19-24]. Highly porous carbon, commonly known as carbon aerogels (CAs) and carbon cryogels (CCs) has been widely investigated [25-28] since 1989 when they were firstly synthesized by Pekala [25]. The CAs and CCs were prepared based on supercritical drying and freeze drying, respectively. Similar to CAs [29], CCs offer a number of advantages or benefits over the activated carbon derived from natural biomass, for example, adjustable porous structure including pore diameter, porosity, specific surface area, good electron conduction pathway, and superior mechanical stability [28]. In addition, CCs offer the ability to control the impurity and adjust the bulk surface chemistry [30]. Up to now, most published research on CCs focused on the aspects of their synthesis methods, structural and property characterizations, as well as their application in energy-storage, such as supercapacitors [27,31-34] and LIBs [35-37].

It is well known that carbon is a typical anode material for LIBs consisting of mesocarbon microbeads and $LiCoO_2$. However, the theoretical specific capacity of carbon is only about 372 mA h/g, which lags behind the demand of rapidly advanced electronics that require batteries with high energy density. Although graphene sheets can potentially host more Li^+ with a specific capacity reaching as high as 744 mA h/g by forming a compound of LiC_6 on both sides [38], the synthesis of graphene sheets is time-consuming and costly, making it difficult for wide-spread industrial applications [39,40]. Conversely, CCs could be prepared efficiently at large-scale with relatively low-cost. Generally, CCs are highly porous with large specific surface area. These characteristics are helpful to the transfer of both electron and Li^+, resulting in a high rate capacity. However, the volumetric capacities and energy density of CCs decrease appreciably because of their relative low density. Therefore, improving the specific capacities of CCs-based materials for LIBs is of great significance.

Efforts have been made to enhance the Li^+ insertion properties of CCs-based materials. For example, CCs-Si composites were prepared by simply adding Si nanoparticles to the water phase during the inverse emulsion polymerization of resorcinol with formaldehyde [37]. Another example is the modification of CCs with SiO powders via a high energy mechanical ball-milling route that could deliver a discharge capacity of 539 mA h/g after 30 cycles [36]. In those work, particles (Si or SiO) were not present in the pores of the CCs, resulting in the volumetric increase of the composites and capitalizing on little synergistic effects of intimate mixing of carbon with Si or SiO or other materials. Therefore, more efforts should be made to improve the properties of CCs-based materials, including the design and the synthesis of tin-carbon composites because of their high theoretical capacity.

The solution impregnation has been used to prepare carbon-tin oxide (or tin) composites [41-44]. For example, organometallic tin source tributylphenyltin solution was impregnated into porous carbon to synthesize carbon-tin composites [41,42]. $SnCl_4$ and $Sn(CH_3COO)_2$ also were employed to prepare carbon-tin (or tin oxide) composites [43,44]. However, those reagents are either expensive or easy to introduce the impurity of chlorine. In this study, CCs were modified by SnO_2 nanoparticles via a simple solution impregnation-calcination method using $SnSO_4$ as the tin sources. The experimental results demonstrated that SnO_2 particles with average diameter of 15 nm, were homogeneously dispersed throughout the CCs to form CCs-SnO_2 nanocomposites (CTs). The SnO_2 nanoparticles are homogenously dispersed in the pores of the CCs, and there is no volume change due to the addition of SnO_2 nanoparticles. The effects of the surface area, pore volume, and pore diameter of the CCs on the electrochemical properties of the CTs were investigated in detail. As anode materials for LIBs, the nanocomposites showed higher discharge capacity, enhanced cyclic stability and improved rate capacity as compared with those of both CCs and pure SnO_2. The synergistic effects between the two components in the CTs may be credited for the superior properties. It is believed that this efficient method will be of great benefit to the synthesis of other metal oxide-CCs composites for a range of applications.

Experimental

Preparation of CCs

CCs were prepared by using resorcinol, furaldehyde, hexamine and tert-butanol as raw materials. The procedure for the synthesis of CCs from resorcinol-furaldehyde gels was similar to previous papers [31]. Three kinds of CCs with different pore sizes, specific surface area, and pore volume were prepared to investigate their effect on the microstructure and properties of the composites. A typical procedure is briefly described as follow. Firstly, the resorcinol and furaldehyde were mixed together at a constant molar ration of 1:2. Then, a proper amount of solvent (tert-butanol) was added in the above mixture, followed by the addition of hexamine as the catalyst. A small amount of deionized water can also be added if necessary. Thirdly, the mixture was sealed and cured in an oven at 353 K for 7 days to complete the gelation process. After that, the gels were dried under vacuum at 223 K in a Labconco FreeZone 1 L freeze dryer. Finally, the dried samples were pyrolyzed in N_2 at 1173 K for 6 h to remove unwanted organic matter and achieve CCs. Sample preparation of the CCs with different microstructures and surface area is summarized in Table 1.

Synthesis of CTs

The solution impregnation-calcination method for the modification of CCs is described as follow. Firstly, CCs were impregnated with saturated solution of $SnSO_4$ in ethanol at 293 K. Secondly, the samples were dried in a freeze dryer for 12 h. Finally, the dried samples were calcined in N_2 at 723 K for 1 h. To improve the mass ratio of SnO_2 in the composites, the impregnation-calcination cycle was repeated for two or three times. After three cycles, the pore volume of the composites was very small. It was not easy to hold the solution of $SnSO_4$ and improve the mass ratio of SnO_2 in composites. Pure SnO_2 powders were prepared by calcining the CTs of C-2 in air at 773 K for 1 h.

Table 1 Chemicals and their usage for CCs.

ID	Furaldehyde (mL)	Resorcinol (g)	Tert-butanol (mL)	Hexamine (g)	Water (mL)
C-1	2.307	1.515	9.692	0.039	1
C-2	3.845	2.525	10.63	0.064	-
C-3	3.076	2.020	12.92	0.051	-

Table 2 Surface areas, pore volumes, and pore diameters of CCs.

Samples	Surface area (m^2/g)			Pore volume (cm^3/g)		Pore diameter (nm)	
	Total	Meso-[a]	Micro-[b]	Meso-	Micro-	Meso-	Micro-
C-1	448	93.6	314	0.408	0.176	4.19	1.14
C-2	481	198	258	0.826	0.143	3.20	1.26
C-3	473	142	276	0.744	0.154	3.63	1.24

[a] Mesopore
[b] Micropore

Characterization

The composites were characterized by powder X-ray diffraction (XRD) on a D8 Bruker X-ray diffractometer with Cu K_α irradiation (λ=0.15406 nm). The microstructure and morphology of the composites were analyzed using a JEOL JSM-7000F scanning electron microscope (SEM), and a FEI Tecnai G2 F20 transmission electron microscope (TEM) operating at 200 kV accelerating voltage. Elemental analysis of samples was achieved using energy dispersive spectroscopy (EDS) analysis was also carried out. Thermogravimetric analysis (TGA) data were collected on a Netzsch STA449C. Nitrogen sorption isotherms were measured by a Quantachrome NOVA 4200e.

Electrochemical measurements

The electrochemical properties of the products were measured using CR2016-type coin cells [45]. In the process of fabricating the half-cells, electrodes were prepared by compressing a mixture of active materials (including the CCs, CTs, pure SnO_2 and mixture of CCs, and pure SnO_2) (80 wt%), carbon black (10 wt%), and polyvinylidene fluoride (10 wt%) on pure copper foil. A Celgard 2400 microporous polypropylene membrane was used as a separator. The electrolyte consisted of a solution of 1 M $LiPF_6$ in ethylene carbonate/dimethyl carbonate (1:1, in volume). Pure lithium foil was used as the counter and reference electrodes. These cells were assembled in an argon-filled glovebox. The discharge and charge measurements were carried out using an Arbin BT2000 system with the cut off potentials being 0.01 V for discharge and 2 V for charge. An electrochemical impedance spectroscopy study was carried out by a Solartron 1260 impedance/gain-phase analyzer, where frequency was varied from 100 kHz to 0.05 Hz.

Results and discussion

Characterization of three kinds of CCs and corresponding CTs

Nitrogen sorption was employed to characterize the surface area, pore volume, and pore diameter of three kinds of CCs (marked as C-1, C-2, and C-3) prepared under different conditions. The experimental procedure of these samples was described in Supporting Information. The nitrogen sorption isotherms of samples C-1, C-2, and C-3 are shown in Fig. S1a-c, respectively. The corresponding data are summarized in Table 2. The sample C-2 possesses the highest mesopore surface area and lowest micropore surface area, with a total surface area of 481 m^2/g, which is the largest amongst all three samples. Besides, the mesopore volume of C-2 is much larger than that of both C-1 and C-3, while its micropore volume is the smallest. Thus, CCs with different surface area and pore size could be prepared by adjusting the experimental parameters, and the controllable synthesis of CCs for various proposes is realizable.

The SEM image of C-2 is displayed in Fig. 1a, where it is clear that C-2 is composed of many small nanoparticles. The carbon particles with a diameter less than 30 nm connect with one another to form aggregates. It should be noted that there are some pores among the aggregates, which are benefit for the loading of SnO_2. The CTs prepared from C-1, C-2, and C-3 with three cycles were marked as CTs♯1-3, CTs♯2-3, and CTs♯3-3, respectively. XRD analysis was employed to detect the crystal phase of the samples, and the results are shown in Fig. 1b. The diffraction peaks of the CCs (C-2) are obscure except for a convexity between 14° and 26°, implying that the CCs are amorphous carbon, which is in good agreement with our earlier work and other literature [35,46]. The sample CTs♯2-3 shows three obvious diffraction peaks at 26.48°, 33.72°, and 51.60°.

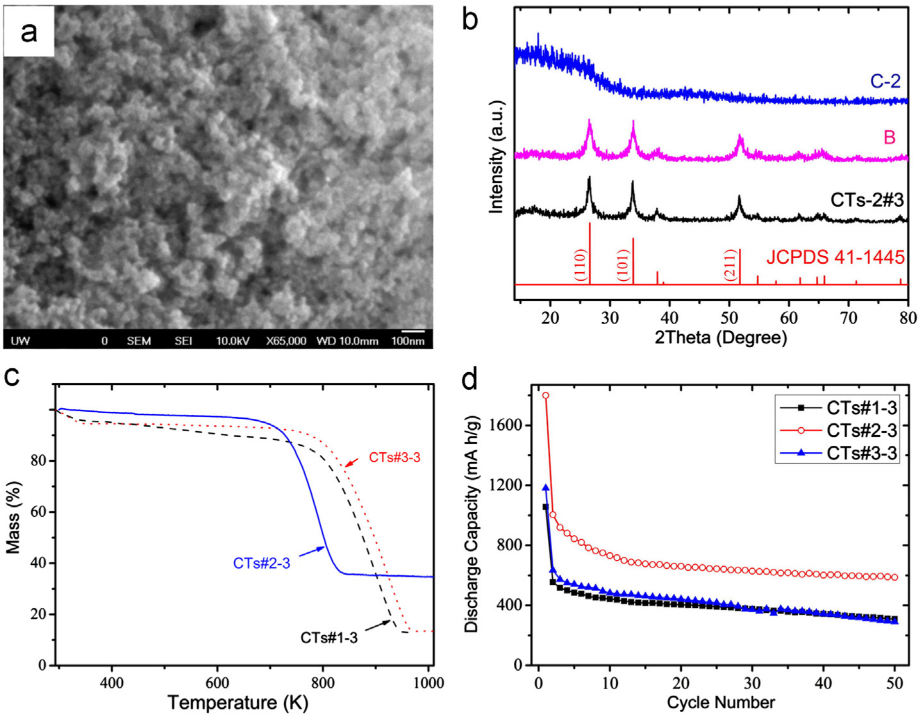

Fig. 1 (a) SEM image of CCs (sample C-2); (b) XRD patterns of CCs (C-2), sample B, CTs-2♯3, and JCPDS 41-1445 of SnO_2 crystallite; (c) TGA curves of samples CTs♯1-3 (dash), CTs♯2-3 (solid) and CTs♯3-3 (dot); (d) Discharge capacities and cyclic stability of samples CTs♯1-3 (solid square), CTs♯2-3 (hollow cycle), and CTs♯3-3 (solid triangle) at a current density of 0.1 A/g.

The standard powder diffraction file data of SnO_2 (41-1445) is shown at the bottom of Fig. 1b. It is clear that the diffraction patterns and relative intensities of the three CTs♯2-3 peaks match well with those of SnO_2, demonstrating that the CCs were modified by SnO_2 via the impregnation-calcination method. According to the Scherrer equation [47], the diameter of the SnO_2 nanoparticles was calculated to be 14.6 nm based on the diffraction peak at 26.48°. It should be noted that no peaks indexed to $SnSO_4$ are found, further suggesting the exhaustive transformation of $SnSO_4$ to SnO_2. A mechanism is proposed based on above results, as displayed in Eq. (1). The broad convexity between 14° and 26° demonstrates the presence of CCs in CTs♯2-3. The weak convexity in the XRD patterns of CTs-2♯3 could be attributed to the relative high intensity of SnO_2 nanoparticles. After calcining CTs-2♯3 in air, a white powder with yellowish hue was achieved. Its XRD patterns are shown as the curve B of Fig. 1b. Comparison with JCPDS 41-1445 suggests that it is pure SnO_2 with the tetragonal crystal system.

$$SnSO_4 \overset{450\,^{\circ}C}{\Rightarrow} SnO_2 + SO_2 \tag{1}$$

To evaluate the weight ratio of the SnO_2 in composites, TGA experiments were carried out at a heating rate of 10 K/min in air with a flow rate of 10 mL/min, the results of which are shown in Fig. 1c. The weight loss below 380 K could be attributed to the elimination of absorbed/trapped water molecules [48]. The sharp weight loss between 700 and 950 K are ascribed to the oxidation of the CCs [49]. The final products obtained from TGA experiments are demonstrated to be SnO_2 by XRD. Therefore, the mass ratio of SnO_2 in CTs♯2-3 was about 35%, much higher than those of CTs♯1-3 and CTs♯3-3. This means that the C-2 CCs may be the most suitable substrate for the host of SnO_2 nanoparticles. Taking into account the surface area results, it can be concluded that CCs with high surface area, large mesopore volume, smaller mesopore diameter are of benefit for the modification of SnO_2. Another apparent difference among those composites is that the temperature corresponding to the oxidation of CCs in CTs♯2-3 is lower than those of the other composites, revealing a high reactivity towards oxygen.

Nitrogen sorption was used again to characterize the composites, and the corresponding results are displayed in Table 3. It is obvious that the relative values of CTs are consistent with those of the CCs, showing the strong effect of the CCs on the loading of SnO_2. Owing to their largest mesopore surface area, the total surface area of CTs♯2-3 is about 290 m^2/g, much higher than that of both CTs♯1-3 and CTs♯3-3. In addition, the mesopore surface area of this sample is also the largest. The mesopore volumes of CTs♯1-3, CTs♯2-3, and CTs♯3-3 are 0.257, 0.514 and 0.355 cm^3/g, respectively. The biggest micropore diameter and smallest mesopore diameter are also found in CTs♯2-3, which are 1.42 and 3.19 nm, respectively Therefore, the large surface area and pore volume of CTs♯2-3 may be attributed with its low thermal stability in air, demonstrated by the TGA results.

Electrochemical experiments towards the storage of Li^+ were carried out to evaluate the properties of the composites. Fig. 1d shows the Li^+ storage discharge capacities and cyclic stability of samples CTs♯1-3, CTs♯2-3, and CTs♯3-3 at a current density of 0.1 A/g. The initial discharge capacity of CTs♯2-3 is about 1800 mA h/g, and only 1056 and 1181 mA h/g for CTs♯1-3 and CTs♯3-3, respectively. The irreversible

Table 3 Surface areas, pore volumes, and pore diameters of the composites.

Samples	Surface area (m^2/g)			Pore volume (cm^3/g)		Pore diameter (nm)	
	Total	Meso-[a]	Micro-[b]	Meso-	Micro-	Meso-	Micro-
CTs♯1-3	202	73.2	121	0.257	0.068	5.97	1.26
CTs♯2-3	293	153	106	0.514	0.060	3.19	1.42
CTs♯3-3	226	89.0	95.9	0.355	0.054	5.42	1.38

[a] Mesopore
[b] Micropore

Table 4 Summarization of the mesopore data for C-2, CTs♯2-1, CTs♯2-2, and CTs♯2-3.

Sample	Surface area (m^2/g)	Pore volume (cm^3/g)	Pore diameter (nm)
C-2	198	0.826	3.20
CTs♯2-1	197	0.759	3.19
CTs♯2-2	170	0.631	3.19
CTs♯2-3	153	0.514	3.19

capacity in the first cycle could be attributed to the deposition of SnO_2 and the formation of the solid electrolyte interphase (SEI) film [50]. Thus, the high initial discharge of CTs♯2-3 could be ascribed to the high surface area, and weight ratio of SnO_2. Another reason for the large irreversible capacity is that only part of the inserted Li^+ can be extracted from the micropores, especially the micropores with diameters less than 0.7 nm [51]. Correspondingly, CTs♯2-3 with the largest surface area and the highest mass ratio of SnO_2 show the highest initial discharge capacity. After 50 cycles, the discharge capacity of CTs♯1-3, CTs♯2-3 and CTs♯3-3 decrease to 308, 587 and 268 mA h/g, respectively. The highest discharge capacity of the CTs♯2-3 could be ascribed to three possible reasons. Firstly, the mass ratio of SnO_2 (with a theoretical capacity as high as 780 mA h/g.) in CTs♯2-3 is the largest among them. Secondly, the pore volume of the CTs♯2-3 is much larger, which is of benefit for the accommodation of volume change during lithiation/delithiation cycles. This could partly prevent the pulverization of SnO_2, resulting in an improved property [52]. Thirdly, more Li^+ could be extracted from the micropores with relative large diameters [51]. Hence, CTs♯2-3 were investigated in detail in the following research.

Structural characterization and Li^+ storage properties of the sample CTs♯2-3 in detail

The samples made from C-2 following one, two, and three cycles of the impregnation-calcination route were designated as CTs♯2-1, CTs♯2-2, and CTs♯2-3, respectively. To characterize the effects of the processing cycles on the porous structure of the nanocomposites (CTs), nitrogen sorption was used again and the isotherm curves are shown in Fig. S2. Those curves are similar to each other, indicating little or no change of the CCs framework. The detail data of C-2, CTs♯2-1, CTs♯2-2, and CTs♯2-3 are summarized in Table 4. Their largest absorption volume reduced from 644 cc/g (for C-2) to 395 cc/g (for CTs♯2-3), showing the decrease of the pore volume. Because micropores could lead to an irreversible Li^+ storage [38,53,54], the research was focused on the mesopore. As shown in Table 4, the mesopore surface area reduces from 198 to 153 m^2/g, along with the rise of the tin oxide mass ratio in the CTs. The mesopore volume also decreases from 0.826 to 0.514 cm^3/g, showing that the SnO_2 nanoparticles are loaded into the mesopores and not the outside of the CCs. Therefore, the larger the CCs mesopore volume has, the higher the SnO_2 weight ratio in CTs is. The consistency of the mesopore diameter demonstrates that the mesopores are not sealed after the insertion of SnO_2 nanoparticles. It should be noted that the specific surface area and specific volume of the composites are closely related to their density. In our case, SnO_2 nanoparticles were loaded in the pores of the CCs without a distinct volume change. In other words, the density of the CTs is higher than that of the CCs. If the specific surface area of the SnO_2 nanoparticles and CCs were calculated separately, they would be 61 m^2/g for SnO_2 nanoparticles (based on the diameter of 15 nm, as shown in Eq. (S1)) and 202 m^2/g for CCs (calculated according to Eq. (S2)). Obviously, the surface area of the CCs (C-2) is nearly unchanged after the SnO_2 loading, when compared with its initial value of 198 m^2/g. In addition, the pore volume of CTs♯2-3 would be 0.791 cm^3/g if the volume of SnO_2 in the composites was neglected and the weight of SnO_2 was deducted. The pore volume change of the CCs also is very small. The nearly unchanged surface area and volume provide further evidence that SnO_2 nanoparticles were deposited on the CCs, and the CCs are of good stability. Besides, CTs will be of improved properties compared with CCs.

The CTs♯2-3 were characterized by SEM and the EDS, as shown in Figs. 2 and S3. An aggregate with a diameter of approximately 15 μm is found on Al foils, and was composed of small particles. The corresponding EDS spectra are displayed in Fig. 2a, and demonstrate that it is primarily composed of three elements, including carbon, oxygen, and tin (aluminum was

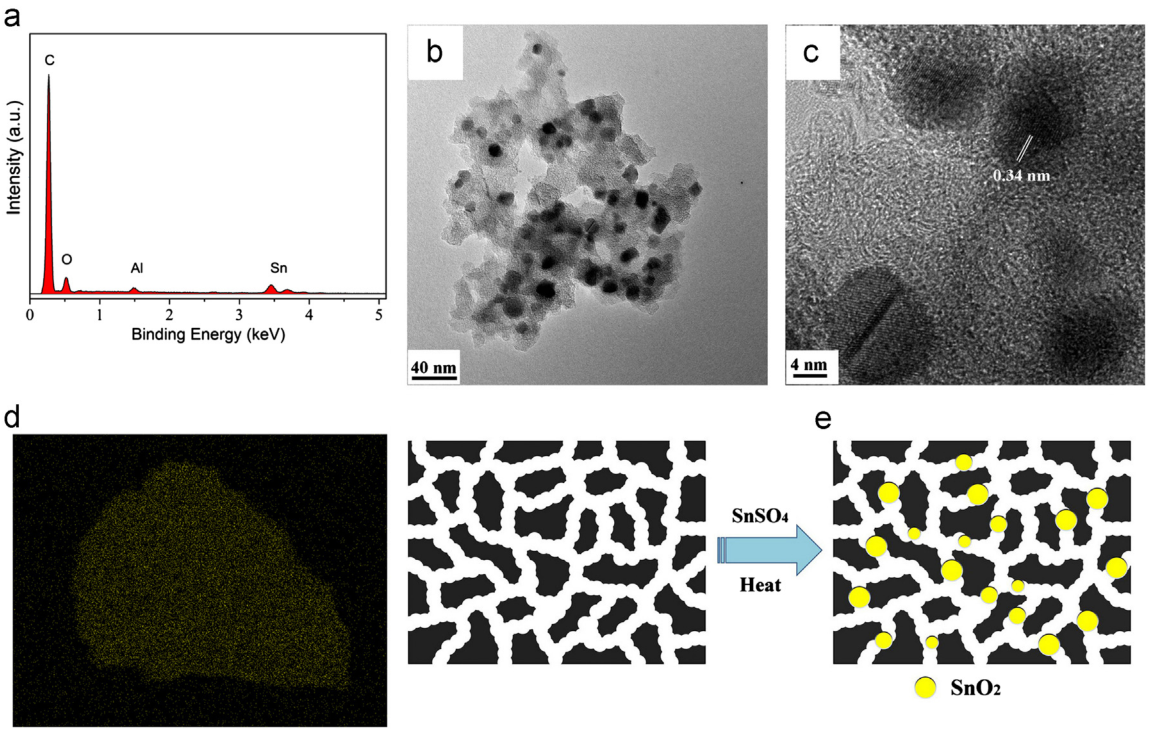

Fig. 2 (a) EDS spectra of the sample CTs#2-3;(b) element mapping of tin in a particle of CTs#2-3; (c) and (d) TEM images of sample CTs#2-3 at different magnifications; (e) simplistic schematic illustration of the formation of CTs.

detected from the Al substrate). No signal corresponding to sulfur is found, indicating the complete transformation of $SnSO_4$ to SnO_2 (Eq. (1)) nearly without any impurities of sulfur. A corresponding element mapping of tin was displayed in Fig. 2b, indicating the homogenous distribution of the SnO_2 in the CTs#2-3 aggregate.

The microstructure of CTs#2-3 was characterized by TEM and the images are displayed in Fig. 2c and d. The TEM image at a low magnification (Fig. 2c) shows that both the CCs and SnO_2 nanoparticles are visible. The particles with darker color are identified as SnO_2, which are loaded onto the CCs. It is clear that the SnO_2 nanoparticles are scattered uniformly on CCs. A high resolution image in Fig. 2d demonstrates that the average diameter of the SnO_2 is approximately 15 nm. This value is smaller than the average pore size of C-2. However, it should be noticed that the pore size of 3.19 nm is an average value. There are some pores with diameters larger than it. So, SnO_2 with diameters of 15 nm could be incorporated into the pores of CCs. The high resolution image also shows regular lattice fringes with a spacing of 0.34 nm, which is highly consistent with the *d* value of the (110) plane of SnO_2 (JCPDS 41-1445). No clear lattices fringes are observed for the CCs, showing the low crystallinity of the CCs. This result matched well with that of XRD, which demonstrated that CCs are successfully modified by small SnO_2 nanoparticles. Based on these results, the synthesis mechanism of the CTs was proposed, as displayed in Fig. 2e. The CCs with porous structure were impregnated with the ethanol solution of $SnSO_4$. Then, they were calcined in N_2 after being freeze dried, gaining CTs with a structure of decorating CCs by SnO_2 nanoparticles. It should be noted that the microstructure of the nanocomposites developed in the present study is sharply different from that reported in literature [35,55]. The porous carbon was coated by a layer of nanoribbons, nanorods or nanoparticles in Pan's and Fischer's investigations [35,55]. On the contrary, oxides nanoparticles were dispersed inside CCs pores with some space among them in our case. Considering the huge volume change of SnO_2 during lithiation/delithiation, the spacing distribution among the SnO_2 nanoparticles are helpful to prevent the pulverization of nanoparticles, resulting in a good structural stability of the nanoparticles and superior cyclic stability [52].

Coin cells were assembled to characterize the electrochemical property of CTs, CCs and SnO_2, and the results are shown in Fig. 3. Fig. 3a shows the first discharge-charge curves of CTs#2-3 and C-2. The CTs#2-3 exhibits a large initial discharge and charge capacities of 2030 and 920 mA h/g, corresponding to a Coulombic efficiency of about 45%. There is an obvious plateau at around 0.8 V, which is well known as the reaction of SnO_2 with lithium to form amorphous Li_2O and the formation of SEI films [50]. The voltage drops fast and a plateau appears at about 1.2 V during the first discharge process of both CTs#2-3 and C-2. This voltage drop could be ascribed to the irreversible insertion of Li^+ into deep-seated superfine micropores [51]. The initial discharge capacity and Coulombic efficiency of C-2 are about 1650 mA h/g and 22%, respectively. The Coulombic efficiency is lower than those of CTs#2-3 and previous reports [36], which could be attributed to the large surface area and mesopocyclicrous structure. The plateau at about 0.8 V during the discharge process could also be found in that of C-2, which is ascribed to the formation of the SEI film. The profiles of C-2 are similar to that of a previous report, showing the typical electrochemical characteristics of CCs [36].

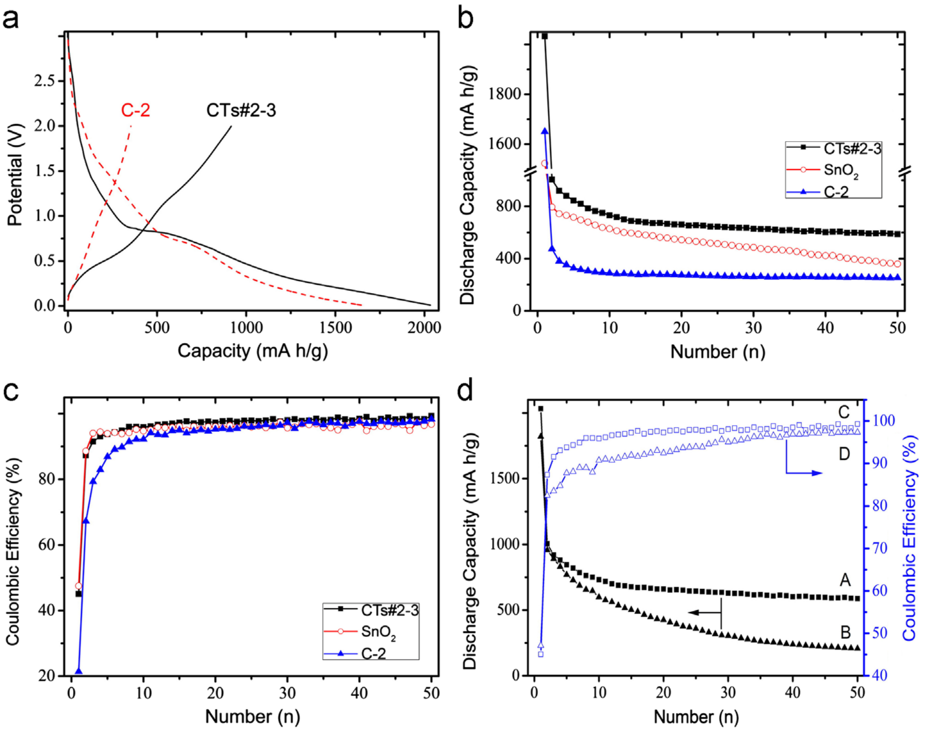

Fig. 3 (a) Discharge and charge curves of CTs#2-3 and C-2 in the first cycle; (b) The cyclic properties of CTs#2-3, pure SnO_2, and CCs (C-2); (c) A plot of the Coulombic efficiencies of CTs#2-3, pure SnO_2, and CCs (C-2); (d) Cyclic properties and the Coulombic efficiencies of CTs#2-3 (A, C) and M-CTs (B, D).

Fig. 3b compares the cyclic property of CTs#2-3, pure SnO_2, and the CCs (C-2). The cyclic property was evaluated at a current density of 0.1 A/g, except the first cycle, in the voltage window of 0.01–2 V. The initial discharge capacity of C-2 is 1650 mA h/g, and fades quickly to 326 mA h/g after 5 cycles and decreases gradually to 250 mA h/g in the 50th cycles. The discharge capacity of pure SnO_2 is 716 mA h/g. However, it reduces quickly to 360 mA h/g after 50 cycles. CTs#2-3 could deliver a discharge capacity of 730 mA h/g in the 10th and 590 mA h/g in the 50th cycle. It is clear that the specific capacity and cyclic stability of CTs#2–3 are better than both pure SnO_2 and CCs (C-2). Besides, this value is also higher than those of carbon–tin oxide (or tin) composites in previous publications [41–43]. The improvement could be attributed to the combined contribution of SnO_2 with high theoretical capacity and the CCs framework with good stability and electrical conductivity.

The Coulombic efficiencies of the three different materials are shown in Fig. 3c. The initial Coulombic efficiency of both pure SnO_2 and CTs#2-3 are about 47%, while it is only about 22% for C-2. The relatively low Coulombic efficiencies are ascribed to the decomposition of SnO_2, the formation of SEI films, and irreversible insertion of Li^+ into the micropores [50]. In the following cycles, the Coulombic efficiencies of CTs#2-3 are about 98%, higher than those of pure SnO_2 and C-2, showing a good cyclic stability of CTs#2-3. Therefore the electrochemical property of the CCs towards the storage of Li^+ is improved by modification with SnO_2 nanoparticles.

To investigate the effect of the microstructure of CTs#2-3 on their electrochemical properties, comparative experiments were carried out and the results are displayed in Fig. 3d. CCs (C-2) were mechanically mixed with SnO_2 with a mass ratio of 6:4 to form hybrids which were marked as M-CTs. As shown in Fig. 3d, M-CTs could deliver an initial discharge capacity of 1820 mA h/g, corresponding to a Coulombic efficiency of 47%. The same parameters are 2050 mA h/g and 45% for CTs#2-3. Their high irreversible capacity is related to the decomposition of SnO_2 to Sn and Li_2O, the formation of SEI films, and irreversible lithiation in micropores [50,51]. The discharge capacities of both CTs#2-3 and M-CTs are about 970 mA h/g in the second cycles. This value is approximately 590 mA h/g for CTs#2–3 after 50 cycles, which is about 2.8 times of that of M-CTs. Additionally, the Coulombic efficiencies of CTs#2-3 during all of 50 cycles, expect the initial one, is higher than those of the M-CTs, indicating a good cyclic stability of CTs#2-3. These results coincide with the fact that CTs#2-3 is not just a simple mixture of CCs and SnO_2.

Scheme 1 shows a possible mechanism to explain why CTs#2-3 exhibits superior electrochemical properties. Firstly, the SnO_2 nanoparticles were loaded on the pore wall of the CCs while the SnO_2 nanoparticles cannot be inserted mechanically into the pores of CCs. So the contribution of the CCs towards the improvement of electronic conductivity is greater in CTs than in M-CTs. Secondly, the nanoparticles embedded pore structure of CTs#2-3 could suppress agglomeration, resulting in good structural stability. Thirdly, the pores could accommodate the volume expansion of tin during the lithiation and prevent the pulverization of tin particles, resulting in a good cyclic property. Fourthly, the connected pores, including the micropores with related large size and mesopores, are of benefit for the transfer of Li^+, reducing the effects of polarization in LIBs.

To evaluate the effect of SnO_2 nanoparticles on the electrochemical property of CCs, rate capacity tests were carried out further. Fig. 4a compares the rate capacities of

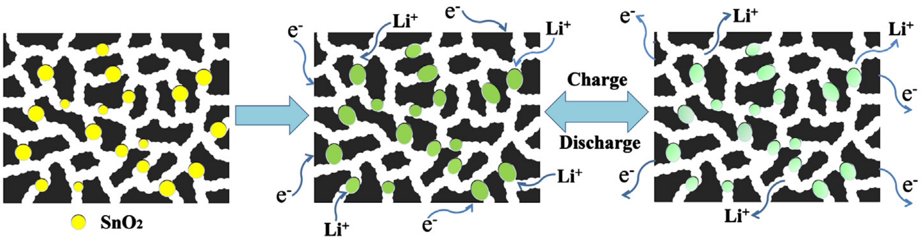

Scheme 1 A schematic illustration that CTs with coherent microstructure are advantageous for the storage of Li$^+$ with improved specific capacity and good cyclic stability.

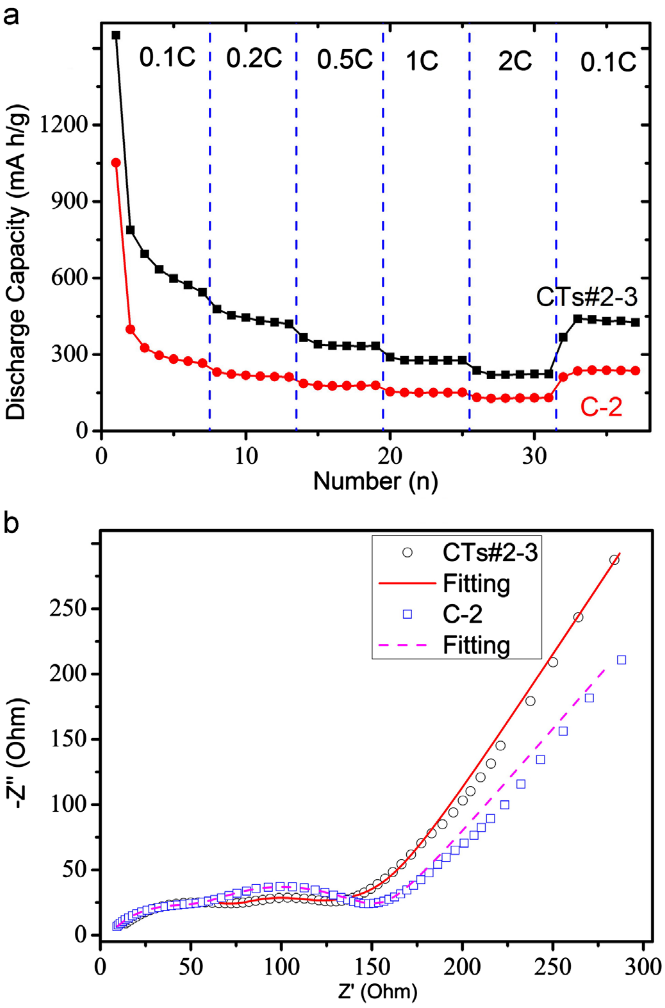

Fig. 4 (a) Rate capacities of CTs♯2-3 and CCs (C-2); (b) AC impendence of CTs♯2-3 (hollow cycles) and CCs (C-2, hollow squares) after rate capacity tests. The lines represent fitting of CTs♯2-3 (the red solid line) and C-2 (the pink dash line) with an equivalent circuit to extract the impedance parameters.

CTs♯2-3 and C-2. C-2 show rather low rate capacity with an average discharge capacity of 290 mA h/g at 0.1 C, 215 mA h/g at 0.2 C, 177 mA h/g at 0.5 C, 150 mA h/g at 1 C, and 128 mA h/g at 2 C. 1 C equals to a current density of 500 mA/g. While CTs♯2-3 exhibit improved discharge capacities of 600, 440, 335, 280, 220 mA h/g at similar rates, respectively. Therefore, the rate capacity of CCs as anode materials for LIBs could also be enhanced effectively by modifying them with SnO_2 nanoparticles. To investigate the reason why CTs♯2-3 have superior properties, the Nyquist plots of the AC impedance for CCs and CTs♯2-3 were measured after the rate capacity tests and the samples were delithiated.

As shown in Fig. 4b, the plots are composed of two partially overlapped semicircles at high- and medium-frequency ranges, and a sloping line at the low-frequency range which represents the Warburg impedance (Z_w) [13,56,57]. The intercept on the Z real axis in the high-frequency range corresponds to the resistance of the electrolyte (R_e). C_f and R_f are the capacitance and resistance of the SEI films (high-frequency). C_{dl} and R_{ct} are the double-layer capacitance and charge-transfer resistance (medium-frequency). The equivalent circuit is shown in Fig. S4.

According to this equivalent circuit, the corresponding fitting curves of both CTs♯2-3 and C-2 are shown in Fig. 4b, and the accurately values are listed in Table S1. It is clear that the R_e of both CTs♯2-3 and C-2 is 7.19 and 5.62 Ω, which are close to each other, showing the consistency of electrolyte. The R_f of CTs♯2-3 is 85.88 Ω, larger than that of C-2 (53.07 Ω). The enhanced resistance could be attributed to the thick SEI films of CTs♯2-3, arising from the huge volume change of tin during lithiation/delithiation cycles. However, the R_{ct} of CTs♯2-3 is 10.2 Ω, much lower than that of C-2 (75.66 Ω), indicating the more facile charge transfer in CTs♯2-3. Therefore, CTs♯2-3 as anode materials for LIBs with lower R_{ct} demonstrate enhanced rate capacity compared with C-2.

Conclusions

The impurity-free nanocomposites with homogenous distribution of SnO_2 nanoparticles in the pores of carbon cryogels can be easily prepared by the impregnation-calcination method based on the thermal decomposition of stannous sulfate. CCs with larger mesopore surface area and pore volume, as well as smaller mesopore diameter, are of benefit for the loading of SnO_2 nanoparticles into the mesopores, and the maximum load of SnO_2 is 35 wt%. Nanocomposites (CTs♯2-3) arising from C-2 could deliver the highest reversible capacity of 590 mA h/g after 50 cycles and excellent cyclic stability with less than 0.82% fading per cycle (except for the first cycle) towards the storage of Li^+. The excellent characteristics of CTs♯2-3 could be attributed to the synergistic effect between CCs and SnO_2, the largest mesopore surface area and pore volume, and smallest mesopore diameter amongst the three samples.

Acknowledgments

This research work has been financially supported in part by the National Science Foundation (NSF, CMMI-1030048) and the University of Washington TGIF grant. Part of this work was conducted at the University of Washington NanoTech User Facility, a member of the NSF National Nanotechnology Infrastructure Network (NNIN). Ming Zhang would like to acknowledge the National Natural Science Foundation of China (21003041 and 21103046), the Hunan Provincial Natural Science Foundation of China (10JJ1011 and 11JJ7004) and the China Scholarship Council.

Appendix A. Supporting information

Supplementary data associated with this article can be found in the online version at http://dx.doi.org/10.1016/j.nanoen.2013.01.009.

References

[1] Z. Fan, Y. Liu, J. Yan, G. Ning, Q. Wang, T. Wei, L. Zhi, F. Wei, Advanced Energy Materials 2 (2012) 419.

[2] Y. Zhai, Y. Dou, D. Zhao, P.F. Fulvio, R.T. Mayes, S. Dai, Advanced Materials 23 (2011) 4828.

[3] L. Wei, G. Yushin, Nano Energy 1 (2012) 552.

[4] T.M. Arruda, M. Heon, V. Presser, P.C. Hillesheim, S. Dai, Y. Gogotsi, S.V. Kalinin, N. Balke, Energy & Environmental Science 6 (2013) 225.

[5] L. Yuan, X.-H. Lu, X. Xiao, T. Zhai, J. Dai, F. Zhang, B. Hu, X. Wang, L. Gong, J. Chen, C. Hu, Y. Tong, J. Zhou, Z.L. Wang, ACS Nano 6 (2011) 656.

[6] X. Li, B. Wei, Nano Energy (2012) http://dx.doi.org/10.1016/j.nanoen.2012.09.008.

[7] D. Cao, Y. Sun, G. Wang, Journal of Power Sources 167 (2007) 250.

[8] M. Zhang, D. Lei, X. Yin, L. Chen, Q. Li, Y. Wang, T. Wang, Journal of Materials Chemistry 20 (2010) 5538.

[9] S.L. Candelaria, Y. Shao, W. Zhou, X. Li, J. Xiao, J.-G. Zhang, Y. Wang, J. Liu, J. Li, G. Cao, Nano Energy 1 (2012) 195.

[10] Z. Chen, D. Zhang, X. Wang, X. Jia, F. Wei, H. Li, Y. Lu, Advanced Materials 24 (2012) 2030.

[11] J. Xiao, D. Mei, X. Li, W. Xu, D. Wang, G.L. Graff, W.D. Bennett, Z. Nie, L.V. Saraf, I.A. Aksay, J. Liu, J.-G. Zhang, Nano Letters 11 (2011) 5071.

[12] L. Ji, H. Zheng, A. Ismach, Z. Tan, S. Xun, E. Lin, V. Battaglia, V. Srinivasan, Y. Zhang, Nano Energy 1 (2012) 164.

[13] Z. Cao, B. Wei, Nano Energy (2012) http://dx.doi.org/10.1016/j.nanoen.2012.11.013.

[14] W.-M. Chen, L. Qie, Y. Shen, Y.-M. Sun, L.-X. Yuan, X.-L. Hu, W.-X. Zhang, Y.-H. Huang, Nano Energy (2012) http://dx.doi.org/10.1016/j.nanoen.2012.11.010.

[15] U. Paulus, T. Schmidt, H. Gasteiger, R. Behm, Journal of Electroanalytical Chemistry 495 (2001) 134.

[16] L. Hu, Y. Cui, Energy & Environmental Science 5 (2012) 6423.

[17] S.W. Lee, N. Yabuuchi, B.M. Gallant, S. Chen, B.-S. Kim, P.T. Hammond, Y. Shao-Horn, Nature Nanotechnology 5 (2010) 531.

[18] M. Heon, S. Lofland, J. Applegate, R. Nolte, E. Cortes, J.D. Hettinger, P.-L. Taberna, P. Simon, P. Huang, M. Brunet, Y. Gogotsi, Energy & Environmental Science 4 (2011) 135.

[19] M. Zhang, B. Qu, D. Lei, Y. Chen, X. Yu, L. Chen, Q. Li, Y. Wang, T. Wang, Journal of Materials Chemistry 22 (2012) 3868.

[20] Y.Q. Zou, Y. Wang, ACS Nano 5 (2011) 8108.

[21] Z.S. Wu, G. Zhou, L.C. Yin, W. Ren, F. Li, H.M. Cheng, Nano Energy 1 (2012) 107.

[22] H.L. Wang, L.F. Cui, Y.A. Yang, H.S. Casalongue, J.T. Robinson, Y.Y. Liang, Y. Cui, H.J. Dai, Journal of the American Chemical Society 132 (2010) 13978.

[23] X. Jia, Z. Chen, A. Suwarnasarn, L. Rice, X. Wang, H. Sohn, Q. Zhang, B.M. Wu, F. Wei, Y. Lu, Energy & Environmental Science 5 (2012) 6845.

[24] S. Chen, P. Bao, G. Wang, Nano Energy (2012) http://dx.doi.org/10.1016/j.nanoen.2012.11.012.

[25] R. Pekala, Journal of Materials Science 24 (1989) 3221.

[26] T. Yamamoto, T. Sugimoto, T. Suzuki, S. Mukai, H. Tamon, Carbon 40 (2002) 1345.

[27] B. Babić, B. Kaluđerović, L. Vračar, N. Krstajić, Carbon 42 (2004) 2617.

[28] T. Yamamoto, A. Endo, T. Ohmori, M. Nakaiwa, Carbon 43 (2005) 1231.

[29] X. Yuan, Y.-J. Chao, Z.-F. Ma, X. Deng, Electrochemistry Communications 9 (2007) 2591.

[30] B.B. García, D. Liu, S. Sepehri, S. Candelaria, D.M. Beckham, L.W. Savage, G. Cao, Journal of Non-Crystalline Solids 356 (2010) 1620.

[31] S.L. Candelaria, B.B. Garcia, D. Liu, G. Cao, Journal of Materials Chemistry 22 (2012) 9884.

[32] A. Szczurek, K. Jurewicz, G. Amaral-Labat, V. Fierro, A. Pizzi, A. Celzard, Carbon 48 (2010) 3874.

[33] B.B. Garcia, S.L. Candelaria, D. Liu, S. Sepheri, J.A. Cruz, G. Cao, Renewable Energy 36 (2011) 1788.

[34] S.L. Candelaria, R. Chen, Y.-H. Jeong, G. Cao, Energy & Environmental Science 5 (2012) 5619.

[35] A. Pan, D. Liu, X. Zhou, B.B. Garcia, S. Liang, J. Liu, G. Cao, Journal of Power Sources 195 (2010) 3893.

[36] Y.J. Chao, X. Yuan, Z.F. Ma, Electrochimica Acta 53 (2008) 3468.
[37] T. Hasegawa, S.R. Mukai, Y. Shirato, H. Tamon, Carbon 42 (2004) 2573.
[38] J.R. Dahn, T. Zheng, Y. Liu, J.S. Xue, Science 270 (1995) 590.
[39] M.J. Allen, V.C. Tung, R.B. Kaner, Chemical Reviews 110 (2010) 132.
[40] D.R. Dreyer, S. Park, C.W. Bielawski, R.S. Ruoff, Chemical Society Reviews 39 (2010) 228.
[41] J. Hassoun, G. Derrien, S. Panero, B. Scrosati, Advanced Materials 20 (2008) 3169.
[42] G. Derrien, J. Hassoun, S. Panero, B. Scrosati, Advanced Materials 19 (2007) 2336.
[43] S.-W. Hwang, S.-H. Hyun, Journal of Power Sources 172 (2007) 451.
[44] M. Egashira, H. Takatsuji, S. Okada, J.-i. Yamaki, Journal of Power Sources 107 (2002) 56.
[45] L. Shen, E. Uchaker, C. Yuan, P. Nie, M. Zhang, X. Zhang, G. Cao, ACS Applied Materials & Interfaces 4 (2012) 2985.
[46] D. Wu, R. Fu, S. Zhang, M.S. Dresselhaus, G. Dresselhaus, Journal of Non-Crystalline Solids 336 (2004) 26.
[47] U. Holzwarth, N. Gibson, Nature Nanotechnology 6 (2011) 534.
[48] M. Zhang, D. Lei, Z. Du, X. Yin, L. Chen, Q. Li, Y. Wang, T. Wang, Journal of Materials Chemistry 21 (2011) 1673.
[49] A. Awadallah-F, A. Elkhatat, S. Al-Muhtaseb, Journal of Materials Science 46 (2011) 7760.
[50] B.J. Li, H.Q. Cao, J.X. Zhang, M.Z. Qu, F. Lian, X.H. Kong, Journal of Materials Chemistry 22 (2012) 2851.
[51] Y.-P. Wu, C.-R. Wan, C.-Y. Jiang, S.-B. Fang, Y.-Y. Jiang, Carbon 37 (1999) 1901.
[52] X.W. Lou, Y. Wang, C. Yuan, J.Y. Lee, L.A. Archer, Advanced Materials 18 (2006) 2325.
[53] Q. Wang, H. Li, L. Chen, X. Huang, Solid State Ionics 152-153 (2002) 43.
[54] Y.S. Hu, P. Adelhelm, B.M. Smarsly, S. Hore, M. Antonietti, J. Maier, Advanced Functional Materials 17 (2007) 1873.
[55] A.E. Fischer, K.A. Pettigrew, D.R. Rolison, R.M. Stroud, J.W. Long, Nano Letters 7 (2007) 281.
[56] M. Umeda, K. Dokko, Y. Fujita, M. Mohamedi, I. Uchida, J. Selman, Electrochimica Acta 47 (2001) 885.
[57] S. Yang, X. Feng, S. Ivanovici, K. Müllen, Angewandte Chemie International Edition 49 (2010) 8408.

Ming Zhang is a Ph. D. Candidate in Hunan University under the direction of Prof. Taihong Wang. Now he also is a visiting student in Prof. Guozhong Cao's group in University of Washington. His research is focused on the synthesis of carbon-based nanocomposites and their application as anodes for lithium ion batteries.

Yanwei Li is a visiting scientist in Prof. Guozhong Cao's group in University of Washington. His research is focused on the design and synthesis of V_2O_5 nanostructures, and their application as cathodes for lithium ion batteries.

Evan Uchaker is a Ph.D. Candidate in the Department of Materials Science and Engineering at the University of Washington under the direction of Prof. Guozhong Cao. His research is focused on the synthesis and characterization of vanadium-based compounds and their application for the cathodes of lithium ion batteries.

Stephanie L. Candelaria is pursuing Ph.D. in the Department of Materials Science and Engineering at the University of Washington under the direction of Prof. Guozhong Cao. Her current research is focused on the sol-gel processing and electrochemical characterization of highly porous carbon from renewable resources for supercapacitors.

Laifa Shen is a visiting student in Prof. Guozhong Cao's group in University of Washington. His research is focused on the design and synthesis of titanium-based compound and their application as anodes for lithium ion batteries.

Dr. Taihong Wang is a Cheung Kong Professor in Hunan University since 2005. His research interests include ultra-sensors, lithium ion batteries, and nanodevices. He has published more than 200 papers, and more than 80 papers were published on the noted journal of Applied Physics Letters in the field of applied physics. More than 50 items of his patents have been authorized.

Dr. Guozhong Cao is a Boeing-Steiner Professor of Materials Science and Engineering, Professor of Chemical Engineering, and Adjunct Professor of Mechanical Engineering at the University of Washington. He has published over 280 papers, 7 books, and 4 proceedings. His recent research is focused mainly on solar cells, lithium-ion batteries, supercapacitors, and hydrogen storage.